LETTER

A large light–mass component of cosmic rays at 10^{17}–$10^{17.5}$ electronvolts from radio observations

S. Buitink[1,2], A. Corstanje[2], H. Falcke[2,3,4,5], J. R. Hörandel[2,4], T. Huege[6], A. Nelles[2,7], J. P. Rachen[2], L. Rossetto[2], P. Schellart[2], O. Scholten[8,9], S. ter Veen[3], S. Thoudam[2], T. N. G. Trinh[8], J. Anderson[10], A. Asgekar[3,11], I. M. Avruch[12,13], M. E. Bell[14], M. J. Bentum[3,15], G. Bernardi[16,17], P. Best[18], A. Bonafede[19], F. Breitling[20], J. W. Broderick[21], W. N. Brouw[3,13], M. Brüggen[19], H. R. Butcher[22], D. Carbone[23], B. Ciardi[24], J. E. Conway[25], F. de Gasperin[19], E. de Geus[3,26], A. Deller[3], R.-J. Dettmar[27], G. van Diepen[3], S. Duscha[3], J. Eislöffel[28], D. Engels[29], J. E. Enriquez[3], R. A. Fallows[3], R. Fender[30], C. Ferrari[31], W. Frieswijk[3], M. A. Garrett[3,32], J. M. Grießmeier[33,34], A. W. Gunst[3], M. P. van Haarlem[3], T. E. Hassall[21], G. Heald[3,13], J. W. T. Hessels[3,23], M. Hoeft[28], A. Horneffer[5], M. Iacobelli[3], H. Intema[32,35], E. Juette[27], A. Karastergiou[30], V. I. Kondratiev[3,36], M. Kramer[5,37], M. Kuniyoshi[38], G. Kuper[3], J. van Leeuwen[3,23], G. M. Loose[3], P. Maat[3], G. Mann[20], S. Markoff[23], R. McFadden[3], D. McKay-Bukowski[39,40], J. P. McKean[3,13], M. Mevius[3,13], D. D. Mulcahy[21], H. Munk[3], M. J. Norden[3], E. Orru[3], H. Paas[41], M. Pandey-Pommier[42], V. N. Pandey[3], M. Pietka[30], R. Pizzo[3], A. G. Polatidis[3], W. Reich[5], H. J. A. Röttgering[32], A. M. M. Scaife[21], D. J. Schwarz[43], M. Serylak[30], J. Sluman[3], O. Smirnov[17,44], B. W. Stappers[37], M. Steinmetz[20], A. Stewart[30], J. Swinbank[23,45], M. Tagger[33], Y. Tang[3], C. Tasse[44,46], M. C. Toribio[3,32], R. Vermeulen[3], C. Vocks[20], C. Vogt[3], R. J. van Weeren[16], R. A. M. J. Wijers[23], S. J. Wijnholds[3], M. W. Wise[3,23], O. Wucknitz[5], S. Yatawatta[3], P. Zarka[47] & J. A. Zensus[5]

Cosmic rays are the highest-energy particles found in nature. Measurements of the mass composition of cosmic rays with energies of 10^{17}–10^{18} electronvolts are essential to understanding whether they have galactic or extragalactic sources. It has also been proposed that the astrophysical neutrino signal[1] comes from accelerators capable of producing cosmic rays of these energies[2]. Cosmic rays initiate air showers—cascades of secondary particles in the atmosphere—and their masses can be inferred from measurements of the atmospheric depth of the shower maximum[3] (X_{max}; the depth of the air shower when it contains the most particles) or of the composition of shower particles reaching the ground[4]. Current measurements[5] have either high uncertainty, or a low duty cycle and a high energy threshold. Radio detection of cosmic rays[6–8] is a rapidly developing technique[9] for determining X_{max} (refs 10, 11) with a duty cycle of, in principle, nearly 100 per cent. The radiation is generated by the separation of relativistic electrons and positrons in the geomagnetic field and a negative charge excess in the shower front[6,12]. Here we report radio measurements of X_{max} with a mean uncertainty of 16 grams per square centimetre for air showers initiated by cosmic rays with energies of 10^{17}–$10^{17.5}$ electronvolts. This high resolution in X_{max} enables us to determine the mass spectrum of the cosmic rays: we find a mixed composition, with a light-mass fraction (protons and helium nuclei) of about 80 per cent. Unless, contrary to current expectations, the extragalactic component of cosmic rays contributes substantially to the total flux below $10^{17.5}$ electronvolts, our measurements indicate the existence of an additional galactic component, to account for the light composition that we measured in the 10^{17}–$10^{17.5}$ electronvolt range.

Observations were made with the Low Frequency Array (LOFAR[13]), a radio telescope consisting of thousands of crossed dipoles with built-in air-shower-detection capability[14]. LOFAR continuously records the radio signals from air showers, while simultaneously running astronomical observations. It comprises a scintillator array (LORA) that triggers the read-out of buffers, storing the full waveforms received by all antennas.

We selected air showers from the period June 2011 to January 2015 with radio pulses detected in at least 192 antennas. The total uptime was about 150 days, limited by construction and commissioning of the
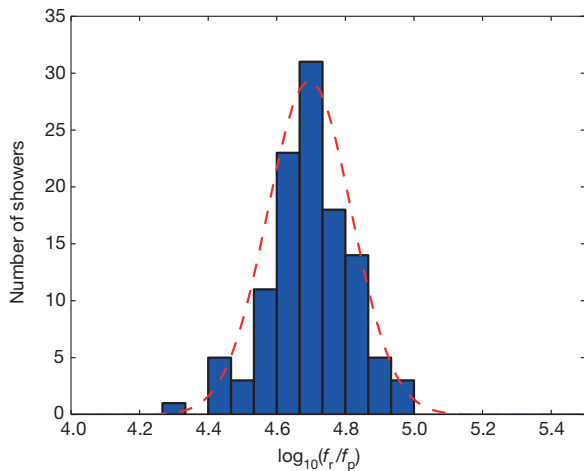
Figure 1 | Energy resolution. The distribution of f_r/f_p (blue bars) is fitted with a Gaussian (red dashed curve), yielding a standard deviation of $\sigma = 0.12$ on a logarithmic scale, which corresponds to an energy resolution of 32%; this value is the quadratic sum of the energy resolution of the radio and particle resolutions. In this analysis, there was no absolute calibration for the received radio power, so f_r has an arbitrary scale.

telescope. Showers that occurred within an hour of lightning activity or that have a polarization pattern that is indicative of influences from atmospheric electric fields are excluded from the sample[15].

Radio intensity patterns from air showers are asymmetric, owing to the interference between geomagnetic and charge-excess radiation. These patterns are reproduced from first principles by summing the radio contributions of all electrons and positrons in the shower. We use the radio simulation code CoREAS[16], a plug-in of CORSIKA[17], which follows this approach.

It has been shown that X_{max}, the atmospheric depth of the shower maximum, can be accurately reconstructed from densely sampled radio measurements[18]. (The atmospheric depth is the air density integrated over the path that the particle has travelled, starting at the top of the atmosphere.) We use a hybrid approach that involves simultaneously fitting the radio and particle data. The radio component is very sensitive to X_{max}, whereas the particle component is used for the energy measurement.

The fit contains four free parameters: the shower core position (x, y), and scaling factors for the particle density (f_p) and the radio power (f_r). If f_p deviates substantially from unity, then the reconstructed energy does not match the simulation and a new set of simulations is produced. This procedure is repeated until the energies agree within the chosen uncertainties. The ratio of f_r and f_p should be the same for all showers, and is used to derive the energy resolution of 32% (see Fig. 1).

The radio intensity fits have reduced χ^2 values ranging from 0.9 to 2.9. All features in the data are well reproduced by the simulation (see Extended Data Figs 1–5), which demonstrates that the radiation mechanism is well understood. The reduced χ^2 values that exceed unity could indicate uncertainties in the antenna response or the atmospheric properties that were not already accounted for, or limitations of the simulation software.

Radio detection becomes more efficient for higher-altitude showers that have larger footprints (that is, larger areas on the ground in which the radio pulse can be detected). However, the particle trigger becomes less efficient because the number of particles reaching the ground decreases. To avoid a bias, we require that all the simulations produced for a shower satisfy a trigger criterion (see Methods). Above 10^{17} eV, this requirement removes four showers from the sample. At lower energies, the number of showers excluded increases rapidly, and so we exclude all showers with energies less than 10^{17} eV from our analysis.

Furthermore, we evaluate the reconstructed core positions of all simulated showers. Showers with a mean reconstruction error greater
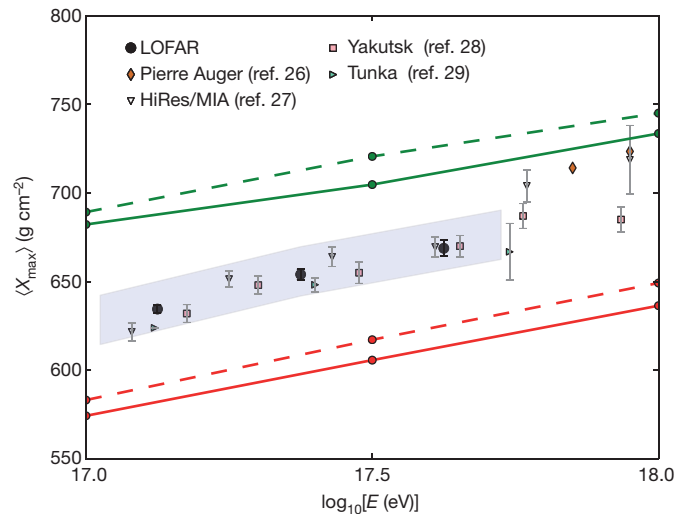

Figure 2 | Measurements of $\langle X_{max} \rangle$. Mean depth of the shower maximum X_{max} as a function of energy E for LOFAR, and for previous experiments that used different techniques[26–29]. Error bars indicate 1σ uncertainties. The systematic uncertainties are $^{+14}_{-10}$ g cm^{-2} on $\langle X_{max} \rangle$ and 27% on E, as indicated by the shaded band. The Pierre Auger Observatory[26] measures the fluorescent light emitted by atmospheric molecules excited by air-shower particles. HiRes/MIA[27] used a combination of this fluorescence technique and muon detection. The Yakutsk[28] and Tunka[29] arrays use non-imaging Cherenkov detectors. The green (upper) lines indicate $\langle X_{max} \rangle$ for proton showers simulated using QGSJETII.04 (solid) and EPOS-LHC (dashed); the red (lower) lines are for showers initiated by iron nuclei.

than 5 m are rejected. This criterion does not introduce a composition bias because it is based on the sets of simulated showers, not on the data. The final event sample contains 118 showers.

The uncertainty in X_{max} is determined independently for all showers[18], and has a mean value of 16 g cm^{-2} (see Extended Data Fig. 6). Figure 2 shows our measurements of the average X_{max}, $\langle X_{max} \rangle$, which are consistent with earlier experiments using different methods. The high resolution for X_{max} per shower allows us to derive more information about the composition of cosmic rays, by studying the shape of the X_{max} distribution. For each shower, we calculate a mass-dependent parameter:

$$a = \frac{\langle X_{proton} \rangle - X_{shower}}{\langle X_{proton} \rangle - \langle X_{iron} \rangle} \tag{1}$$

in which X_{shower} is the reconstructed X_{max}, and $\langle X_{proton} \rangle$ and $\langle X_{iron} \rangle$ are mean values of X_{max} for proton and iron showers, respectively, predicted by the hadronic interaction code QGSJETII.04[19].

The cumulative probability density function (CDF) for all showers is plotted in Fig. 3. First, we fit a two-component model of protons and iron nuclei (p and Fe), with the mixing ratio as the only free parameter. To calculate the corresponding CDFs we use a parameterization of the X_{max} distribution fitted to simulations based on QGSJETII.04. The best fit is found for a proton fraction of 62%, but this fit describes the data poorly, with $p = 1.1 \times 10^{-6}$. (The test statistic for this fit is the maximum deviation between the data and the model CDFs, and p represents the probability of observing this deviation, or a larger one, assuming the fitted composition model; see Methods.)

A better fit is achieved with a four-component model of protons and helium, nitrogen and iron nuclei (p, He, N and Fe), yielding $p = 0.17$. Although the best fit is found for a helium fraction of 80%, the fit quality deteriorates slowly when replacing helium nuclei with protons. This is demonstrated in Fig. 4, in which p is plotted for four-component fits for which the fractions of helium nuclei and protons are fixed, and the ratio of nitrogen and iron nuclei is the only free parameter. The total fraction of light elements (p and He) is in the range [0.38, 0.98] at a 99% confidence level, with a best-fit value of 0.8. The heaviest
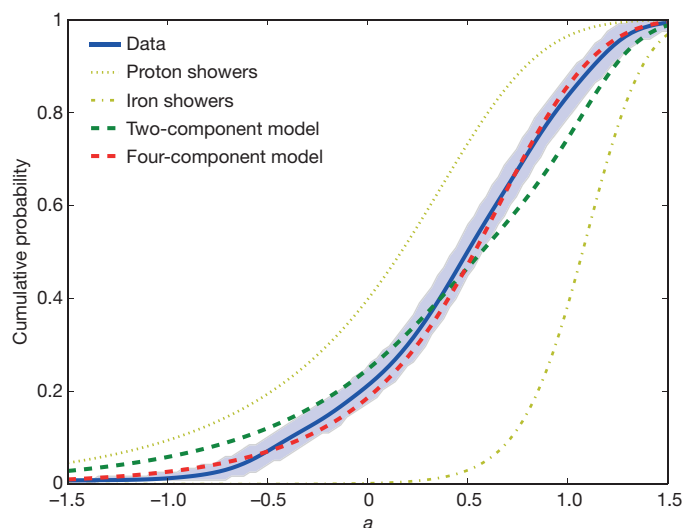
Figure 3 | Composition model fits. The cumulative probability density of the parameter a (see equation (1)) determined from the data (blue line; shading indicates the range in which $p > 0.01$) and several models, on the basis of QGSJETII.04 simulations. The set that contains only proton showers is centred around $a = 0$ and has a large spread (yellow dotted line), whereas iron showers give a distribution with a small spread centred around $a = 1$ (yellow dash-dotted line). A two-component model (p and Fe; green dashed line) yields the best fit for a proton fraction of 62%, but does not describe the data well ($p = 1.1 \times 10^{-6}$). A four-component model (p, He, N and Fe; red dashed line) gives the best fit with 0% protons, 79% helium, 19% nitrogen and 2% iron, with $p = 0.17$. The uncertainty on these values is presented in Fig. 4.

Figure 4 | p-value distribution for the four-component model. The four-component model is explored further by fixing the proton and helium fractions at all possible combinations, and solving for the nitrogen/iron ratio. The p value (see Fig. 3) is plotted as a function of the proton and helium fractions. The optimal fit (largest p value) is found for 0% protons and 79% helium ($p = 0.17$), but the deviation deteriorates slowly when replacing helium with protons. The black contour line bounds all combinations for which $p > 0.01$. At this significance level, the total fraction of light elements (p and He) lies between 0.38 and 0.98.

composition that is allowed within systematic uncertainties has a best-fit light-element fraction of 0.6 and a 99% confidence interval of [0.18, 0.82]. For information about the systematic uncertainties and the statistical analysis, see Methods.

The abundances of individual elements depend on the hadronic interaction model. The X_{max} values predicted by EPOS-LHC[20] are, on average, 15–20 g cm^{-2} higher than those predicted by QGSJETII.04 (see Fig. 2). This coincides with the separation in $\langle X_{max} \rangle$ between, for example, protons and deuterium or between helium and beryllium. Therefore, we present our result as a total fraction of light elements, to avoid placing too much emphasis on individual elements.

Recent results from the Pierre Auger Observatory[3] indicate that the composition of cosmic rays at 10^{18} eV, just below the 'ankle' (a hardening of the all-particle cosmic-ray spectrum), can be fitted with a mixture of protons and either helium (QGSJET.II04) or nitrogen (EPOS-LHC). As the energy decreases, the proton fraction of the cosmic-ray composition decreases while the helium (or nitrogen) fraction increases, down to the threshold energy of 7×10^{17} eV. An extrapolation of this trend to our mean energy of 3×10^{17} eV connects smoothly to our best-fitting solution in which helium dominates.

An 'ankle'-like feature in the cosmic-ray energy spectrum at $10^{17.1}$ eV has been measured[4] at the KASCADE-Grande experiment, at which the spectral index for light elements changes to $\gamma = -2.79 \pm 0.08$. However, the light particle (p and He) fraction is found to be less than 30% at 3×10^{17} eV (on the basis of figure 4 in ref. 4), which is considerably lower than our value. In contrast to LOFAR, the composition measurements presented in ref. 4 are based on the muon/electron ratio. A muon excess compared to all commonly used hadronic interaction models was reported[21]. Inaccurate predictions of muon production, or $\langle X_{max} \rangle$, could be the cause of the discrepancy in the fraction of light particles predicted by LOFAR and KASCADE-Grande.

If the 'knee' in the all-particle cosmic-ray spectrum (a steepening near 3×10^{15} eV) corresponds to the proton or helium cut-off of the main galactic cosmic-ray population, then the corresponding iron cut-off would lie at an energy of at most 26 times larger. If the main
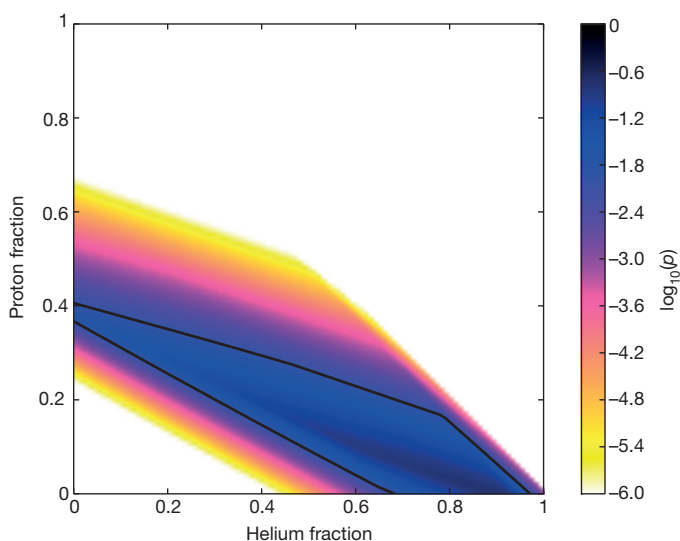
population of galactic cosmic-ray sources still dominates at 10^{17} eV, then the mass composition of the cosmic rays should be dominated by heavy elements at that energy. Therefore, the large component of light elements observed with LOFAR must have another origin.

In principle, it is possible that we observe an extragalactic component. In that case, the 'ankle' in the cosmic-ray spectrum, at energies slightly greater than 10^{18} eV, does not indicate the transition from galactic to extragalactic origin. Instead, it can be explained as the imprint of pair production on the cosmic microwave background on an extragalactic proton spectrum[22]. However, because this feature only appears for a proton-dominated flux it is contrary to our data that indicate a mixture of light elements.

A second galactic component, dominating around 10^{17} eV, could be produced by a class of extremely energetic sources (galactic exatrons), such as the explosions of Wolf Rayet stars into their stellar winds[23] or past galactic gamma-ray bursts[24]. Alternatively, the original galactic population could be reaccelerated by the galactic-wind-termination shock[25]. Such scenarios predict mixtures of light elements, consistent with our results.

1. IceCube Collaboration. Evidence for high-energy extraterrestrial neutrinos at the IceCube detector. *Science* **342,** 1242856 (2013).
2. Murase, K., Ahlers, M. & Lacki, B. Testing the hadronuclear origin of PeV neutrinos observed with IceCube. *Phys. Rev. D* **88,** 121301 (2013).
3. Aab, A. *et al.* Depth of maximum of air-shower profiles at the Pierre Auger Observatory. II. Composition implications. *Phys. Rev. D* **90,** 122006 (2014).
4. Apel, W. *et al.* Ankle-like feature in the energy spectrum of light elements of cosmic rays observed with KASCADE-Grande. *Phys. Rev. D* **87,** 081101 (2013).
5. Kampert, K.-H. & Unger, M. Measurements of the cosmic ray composition with air shower experiments. *Astropart. Phys.* **35,** 660–678 (2012).
6. Allan, H. R. in *Progress in Elementary Particle and Cosmic Ray Physics* Vol. 10 (eds Wilson, J. G. & Wouthuysen, S. A.) 171–302 (North-Holland Pub. Co., 1971).
7. Falcke, H. & Gorham, P. W. Detecting radio emission from cosmic ray air showers and neutrinos with a digital radio telescope. *Astropart. Phys.* **19,** 477–494 (2003).
8. Falcke, H. *et al.* Detection and imaging of atmospheric radio flashes from cosmic ray air showers. *Nature* **435,** 313–316 (2005).

9. Huege, T. The renaissance of radio detection of cosmic rays. *Braz. J. Phys.* **44,** 520–529 (2014).
10. Apel, W. *et al.* Reconstruction of the energy and depth of maximum of cosmic-ray air showers from LOPES radio measurements. *Phys. Rev. D* **90,** 062001 (2014).
11. Belov, K. *et al.* Towards determining the energy of the UHECRs observed by the ANITA detector. *AIP Conf. Proc.* **1535,** 209–213 (2013).
12. Werner, K. & Scholten, O. Macroscopic treatment of radio emission from cosmic ray air showers based on shower simulations. *Astropart. Phys.* **29,** 393–411 (2008).
13. van Haarlem, M. *et al.* LOFAR: the LOw-Frequency ARray. *Astron. Astrophys.* **556,** A2 (2013).
14. Schellart, P. *et al.* Detecting cosmic rays with the LOFAR radio telescope. *Astron. Astrophys.* **560,** A98 (2013).
15. Schellart, P. *et al.* Probing atmospheric electric fields in thunderstorms through radio emission from cosmic-ray-induced air showers. *Phys. Rev. Lett.* **114,** 165001 (2015).
16. Huege, T., Ludwig, M. & James, C. Simulating radio emission from air showers with CoREAS. *AIP Conf. Proc.* **1535,** 128–132 (2013).
17. Heck, D., Knapp, J., Capdevielle, J. N., Schatz, G. & Thouw, T. *CORSIKA: a Monte Carlo code to simulate extensive air showers.* Report No. FZKA 6019 (Forschungszentrum Karlsruhe, 1998).
18. Buitink, S. *et al.* Method for high precision reconstruction of air shower X_{max} using two-dimensional radio intensity profiles. *Phys. Rev. D* **90,** 082003 (2014).
19. Ostapchenko, S. QGSJET-II: results for extensive air showers. *Nucl. Phys. B* **151,** 147–150 (2006).
20. Pierog, T. & Werner, K. EPOS model and ultra high energy cosmic rays. *Nucl. Phys. B* **196,** 102–105 (2009).
21. Aab, A. *et al.* Muons in air showers at the Pierre Auger Observatory: mean number in highly inclined events. *Phys. Rev. D* **91,** 032003 (2015).
22. Aloisio, R. *et al.* A dip in the UHECR spectrum and the transition from galactic to extragalactic cosmic rays. *Astropart. Phys.* **27,** 76–91 (2007).
23. Stanev, T., Biermann, P. & Gaisser, T. Cosmic rays. IV. The spectrum and chemical composition above 10 GeV. *Astron. Astrophys.* **274,** 902–915 (1993).
24. Calvez, A., Kusenko, S. & Nagataki, S. Role of galactic sources and magnetic fields in forming the observed energy-dependent composition of ultrahigh-energy cosmic rays. *Phys. Rev. Lett.* **105,** 091101 (2010).
25. Jokipii, J. R. & Morfill, G. Ultra-high-energy cosmic rays in a galactic wind and its termination shock. *Astrophys. J.* **312,** 170–177 (1987).
26. Letessier-Selvon, A. *et al.* Highlights from the Pierre Auger Observatory. *Braz. J. Phys.* **44,** 560–570 (2014).
27. Abu-Zayyad, T. *et al.* Measurement of the cosmic-ray energy spectrum and composition from 10^{17} to $10^{18.3}$ eV using a hybrid technique. *Astrophys. J.* **557,** 686–699 (2001).
28. Knurenko, S. & Sabourov, A. The depth of maximum shower development and its fluctuations: cosmic ray mass composition at $E_0 \geq 10^{17}$ eV. *Astrophys. Space Sci. Trans.* **7,** 251–255 (2011).
29. Berezhnev, S. F. *et al.* Tunka-133: primary cosmic ray mass composition in the energy range $6 \cdot 10^{15} - 10^{18}$ eV. *Proc. 32nd Int. Cosmic Ray Conf.* **1,** 209–212 (2011).

Author Contributions All authors are part of the LOFAR collaboration and have contributed to the design, construction, calibration and maintenance of LOFAR and/or LORA. The first thirteen authors constitute the Cosmic Ray Key Science Project and have contributed to the acquisition, calibration and analysis of cosmic-ray radio data and LORA data. The manuscript was written by S.B. and subjected to an internal collaboration-wide review process. All authors approved the final version of the manuscript.

Author Information Reprints and permissions information is available at www.nature.com/reprints. The authors declare no competing financial interests. Readers are welcome to comment on the online version of the paper. Correspondence and requests for materials should be addressed to S.B. (Stijn.Buitink@vub.ac.be).

METHODS

Event selection. Cosmic ray detection at LOFAR runs continuously in the background during astronomical observations. When 16 out of the 20 scintillator stations of the LORA particle array detect a signal, a 'trigger' is issued and the ring buffers of all active antennas within about a 1-km radius are stored for offline analysis[14]. Which antennas are active depends on the settings of the astronomical observation. For this analysis, we selected showers that were measured with at least four antenna stations (corresponding to at least 192 antennas) in the low band (30–80 MHz after filtering).

The trigger and selection criteria introduce a composition bias. This bias is removed by excluding certain showers on the basis of dedicated sets of simulations that are produced for each observed shower. Each of these sets contains 50 proton and 25 iron showers that span the whole range of possible shower depths. A shower is only accepted if all simulations in its set satisfy the trigger and selection criteria. This anti-bias exclusion removes many showers below 10^{17} eV, but only four above that energy. Consequently, we restrict our analysis to the higher-energy showers, imposing a minimum bound on the reconstructed shower energy of $E_{reco} = 10^{17}$ eV.

Imposing this energy bound introduces another potential source of compositional bias, because the reconstructed energy might depend on the depth of the shower. However, in our reconstruction approach, this effect is very small because energy and X_{max} are fitted simultaneously. Extended Data Fig. 7 shows distributions of the ratio between true and reconstructed energy for proton and iron simulations. The systematic offset between the two particle types is of the order of 1%.

We used data from the Royal Netherlands Meteorological Institute to check for lightning-storm conditions during our observations. When lightning strikes were detected in the north of the Netherlands within an hour from a detection, the event is flagged and excluded from the analysis. The presence of electric fields in the clouds can severely alter the radio emission even in the absence of lightning discharges[30]. The polarization angle of the radio pulse is very sensitive to the nature of the emission mechanism[15,31] and is used as an additional veto against strong field conditions.

Finally, a quality criterion is imposed on the sample so that only showers that have a core position and arrival direction that allows accurate reconstruction are included. We use the dedicated sets of simulations produced for each shower to derive uncertainties on core position, energy and X_{max}. These three values are highly correlated, so a single criterion based on the core uncertainty of $\sigma_{core} < 5$ m is sufficient.

The quality criterion is based on the dedicated sets of simulations. These sets are produced for a specific combination of core position and arrival direction. Therefore, the quality criterion is effectively a criterion on position and direction, and does not introduce a composition bias.

There is no criterion on the quality of the reconstruction of the actual data. By applying the criteria described above we obtain a sample of 118 showers that are fitted to the simulation yielding reduced χ^2 values in the range 0.9–2.9. Deviations from unity can be ascribed to uncertainties in antenna response, atmospheric properties such as the index of refraction, or limitations of the simulation software.

Reconstruction. The energy and X_{max} of the shower are reconstructed with the technique described in ref. 18.

Statistical uncertainty. The statistical uncertainty on the power measurements of individual antennas includes three contributions. First, there is contribution from the background noise, which is a combination of system noise and the galactic background. Second, there is a contribution from uncertainties in the antenna response model. There can be differences between the responses of antennas, either because of antenna properties (for example, cross-talk between nearby antennas) or because of signal properties (for example, polarization). Because these fluctuations are different for each shower core position and arrival direction, they are essentially random and so are included as a 10% statistical uncertainty on the power. Third, there is a contribution due to the error introduced by interpolating the simulated pulse power. Strictly speaking this is not a measurement uncertainty, but it must be taken into account when fitting the data to simulation. The interpolation error is of the order of 2.5% of the maximum power[18]. The three contributions are added in quadrature and produce the 1σ error bars shown in Extended Data Figs 1–5.

The statistical uncertainty on X_{max} is given by the quadratic sum of the uncertainties due to the reconstruction technique and the atmospheric correction. The former is found by applying our analysis to simulated events with added Gaussian noise, where the noise level is determined from the data.

In the CORSIKA simulations, the standard US atmosphere model was used. The reconstructed shower depth is corrected for variations in the atmosphere using data from the Global Data Assimilation System (GDAS) of the NOAA National Climatic Data Center. We follow a previously developed procedure[32], which typically leads to adjustments of the order of 5–20 g cm^{-2}. The remaining uncertainty after correction is of the order of 1 g cm^{-2}.

The refractive index of air is a function of temperature, air pressure and relative humidity. Using local weather information, the final data were split in two groups of equal size, corresponding to conditions with relatively high or low refractive index. The mean reconstructed X_{max} of these two subsets deviate from that of the total sample by ± 5 g cm^{-2}; we adopt this value as an additional statistical uncertainty. Because the refractivity used in simulation corresponds to dry air, there is also an associated systematic error (see below).

The total statistical uncertainty on X_{max} is found by adding the above factors in quadrature. A distribution of the uncertainty for the showers in our final sample is shown in Extended Data Fig. 6.

The energy resolution is 32% and is found by comparing energy scaling factors of the radio power and particle density fit (see Fig. 1).

Systematic effects. The data have been subjected to several tests (outlined below) to determine the systematic uncertainty on the reconstructed values for X_{max}.

Zenith-angle dependence. The final data are split into two groups of equal size by selecting showers with a zenith angle below or above 32°. For both groups, the mean reconstructed X_{max} is calculated, yielding deviations from the mean value of the complete sample of ± 8 g cm^{-2}. This spread is larger than is expected from random fluctuations alone and is included as a systematic uncertainty. The dependence on zenith angle may be related to atmospheric uncertainties (see below).

Refractive index of air. As explained above, the refractive index changes because of differences in atmospheric conditions. Fluctuations in X_{max} due to changing humidity are of the order of 5 g cm^{-2} with respect to the mean. However, the refractive index that was used in the radio simulations corresponds to dry air, and is a lower bound on the actual value. Therefore, the real value of X_{max} can be higher than the reconstructed value, but not lower; we adopt an asymmetric systematic uncertainty of $+10$ g cm^{-2}.

Hadronic interaction model. Because the reconstruction technique is based on full Monte Carlo simulations, it is sensitive to the choice of hadronic interaction model that is used. A comparison between QGSJETII.04, SYBILL 2.1 and EPOS-LHC, revealed that the uncertainty due to model dependence is about 5 g cm^{-2}. The uncertainty on the composition due to different models (in other words, on how to interpret the measured X_{max} values) is larger.

Radiation code. For this analysis we used the radiation code CoREAS, in which the contributions of all individual charges to radiation field are added together. The advantage of this microscopic approach is that it is completely model-independent and based on first principles. ZHAireS[33] is another microscopic code, which gives very similar results[34]. To calculate the emission, CoREAS uses the end-point formalism[35], whereas ZHAireS is based on the ZHS algorithm[36]. Both formalisms are derived directly from Maxwell's equations and have been shown to be equivalent[37]. The other difference between CoREAS and ZHAires is that they take the particle distribution from different air-shower propagation codes (CORSIKA and AIRES, respectively) that internally use different hadronic interaction models. Because the radiation formalisms themselves are equivalent, small differences between CoREAS and ZHAireS are probably due to differences in the hadronic interaction models used to simulate the particle interactions. Therefore, the choice of radiation code does not introduce additional systematic uncertainty on top of the uncertainty due to hadronic interaction models that is already included. A comparison study with LOFAR data did not show any evidence for a systematic offset between the codes (S.B. *et al.*, in preparation).

The remaining small dependence of X_{max} on zenith angle is possibly related to the refractive index. Showers with different inclination angles have their shower maximum at different altitudes and, therefore, different local air pressures and refractive indices. Consequently, increasing the refractive index used in simulations will result in a zenith-dependent change in reconstructed Xmax. This could potentially remove the observed dependence of the composition on zenith angle. Correctly taking into account a complete atmospheric model for the profile of the refractivity of air is subject of further study. Here, we treat the effect conservatively by linearly adding the first two contributions to the uncertainty. The other two contributions are independent and are added in quadrature, yielding a total systematic uncertainty of $^{+14}_{-10}$ g cm^{-2}.

The systematic uncertainty in the energy reconstruction with the LORA particle detector array is 27%, which includes effects due to detector calibration, hadronic interaction models and the assumed slope of the primary cosmic-ray spectrum in the CORSIKA simulations[38,39].

Statistical analysis. For each observed shower, we calculate a using equation (1):

$$a = \frac{\langle X_{proton} \rangle - X_{shower}}{\langle X_{proton} \rangle - \langle X_{iron} \rangle}$$

in which X_{shower} is the reconstructed X_{max}, and $\langle X_{proton} \rangle$ and $\langle X_{iron} \rangle$ are mean values predicted by QGSJETII.04[19]. Therefore, a is an energy-independent parameter that is mass sensitive. A pure proton composition results in a wide distribution of a

centred around zero, whereas a pure iron composition would results in a narrower distribution centred around one.

From the measurements we construct a cumulative distribution function (CDF) using the following Monte Carlo approach. A realization of the data is made by taking the measured values for the energy and X_{max}, adding random fluctuations based on the statistical uncertainty of these parameters, and calculating a and the corresponding CDF. By constructing a large number of realizations with different random fluctuations, we calculate the mean CDF and the region that contains 99% of all realizations. These are indicated in Fig. 3 as the solid blue line and the shaded region, respectively.

We fit theoretical CDFs on the basis of compositions with two or four mass components to the data. The test statistic in the fit is the maximum deviation between the data and the model CDFs. The p value represents the probability of observing this deviation, or a larger one, assuming the fitted composition model.

We first use a two-component model of proton and iron nuclei, in which the mixing ratio is the only free parameter. The best fit is found for a proton fraction of 62%, but it describes the data poorly, with p value of 1.1×10^{-6}.

A better fit is achieved with a four-component model (p, He, N and Fe), yielding $p = 0.17$. Although the best fit is found for a helium fraction of 80%, the fit quality deteriorates slowly when replacing helium by protons. This is demonstrated in Fig. 4, in which p is plotted for four-component fits with the fractions of helium and proton fixed, and the ratio between nitrogen and iron is the only free parameter. The solid line in Fig. 4 bounds the parameter space in which $p > 0.01$. We construct a 99% confidence interval on the total fraction of light elements (p and He) by finding the two extreme values of this fraction that lie within the $p > 0.01$ region.

The total fraction of light elements (p and He) is in the range $[0.38, 0.98]$ at the 99% confidence level, with a best fit value of 0.8. The heaviest composition that is allowed within systematic uncertainties (see above) has a best-fit p + He fraction of 0.6 and a 99% confidence interval of $[0.18, 0.82]$.

Code availability. Data analysis was done with PyCRTools. PyCRTools is free software, available from http://usg.lofar.org/svn/code/trunk/src/PyCRTools, which can be redistributed and/or modified under the terms of the GNU General Public License as published by the Free Software Foundation, either version 3 of the License or any later version.

30. Buitink, S. *et al.* Amplified radio emission from cosmic ray air showers in thunderstorms. *Astron. Astrophys.* **467,** 385–394 (2007).
31. Schellart, P. *et al.* Polarized radio emission from extensive air showers measured with LOFAR. *J. Cosmol. Astropart. Phys.* **10,** 014 (2014).
32. The Pierre Auger Collaboration. Description of atmospheric conditions at the Pierre Auger Observatory using the Global Data Assimilation System (GDAS). *Astropart. Phys.* **35,** 591–607 (2012).
33. Alvarez-Muñiz, J. *et al.* Monte Carlo simulations of radio pulses in atmospheric showers using ZHAireS. *Astropart. Phys.* **35,** 325–341 (2012).
34. Huege, T. *et al.* The convergence of EAS radio emission models and a detailed comparison of REAS3 and MGMR simulations. *Nucl. Instrum. Methods Phys. Res. A* **662** (Suppl.) S179–S186 (2012).
35. James, C., Falcke, H., Huege, T. & Ludwig, M. General description of electromagnetic radiation processes based on instantaneous charge acceleration in "endpoints". *Phys. Rev. E* **84,** 056602 (2011).
36. Zas, E., Halzen, F. & Stanev, T. Electromagnetic pulses from high-energy showers: implications for neutrino detection. *Phys. Rev. D* **45,** 362–376 (1992).
37. Belov, K. *et al.* Accelerator measurements of magnetically induced radio emission from particle cascades with applications to cosmic-ray air showers. *Phys. Rev. Lett.* (in the press). Preprint at http://arXiv.org/abs/1507.07296 (2015).
38. Thoudam, S. *et al.* LORA: a scintillator array for LOFAR to measure extensive air showers. *Nucl. Instrum. Methods Phys. Res. A* **767,** 339–346 (2014).
39. Thoudam, S. *et al.* Measurement of the cosmic-ray energy spectrum above 10^{16} eV with the LOFAR Radboud Air Shower Array. *Astropart. Phys.* **73,** 34–43 (2016).
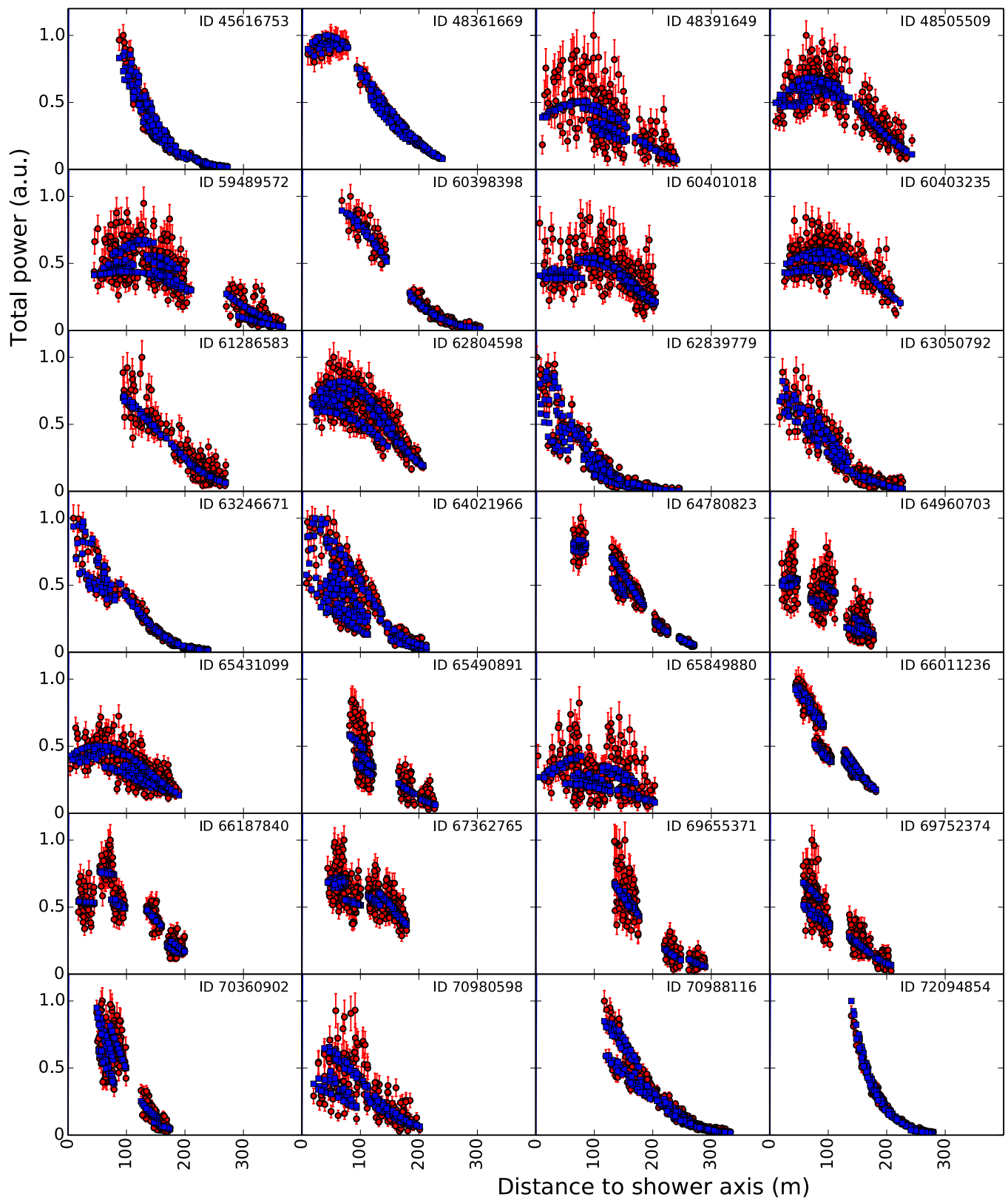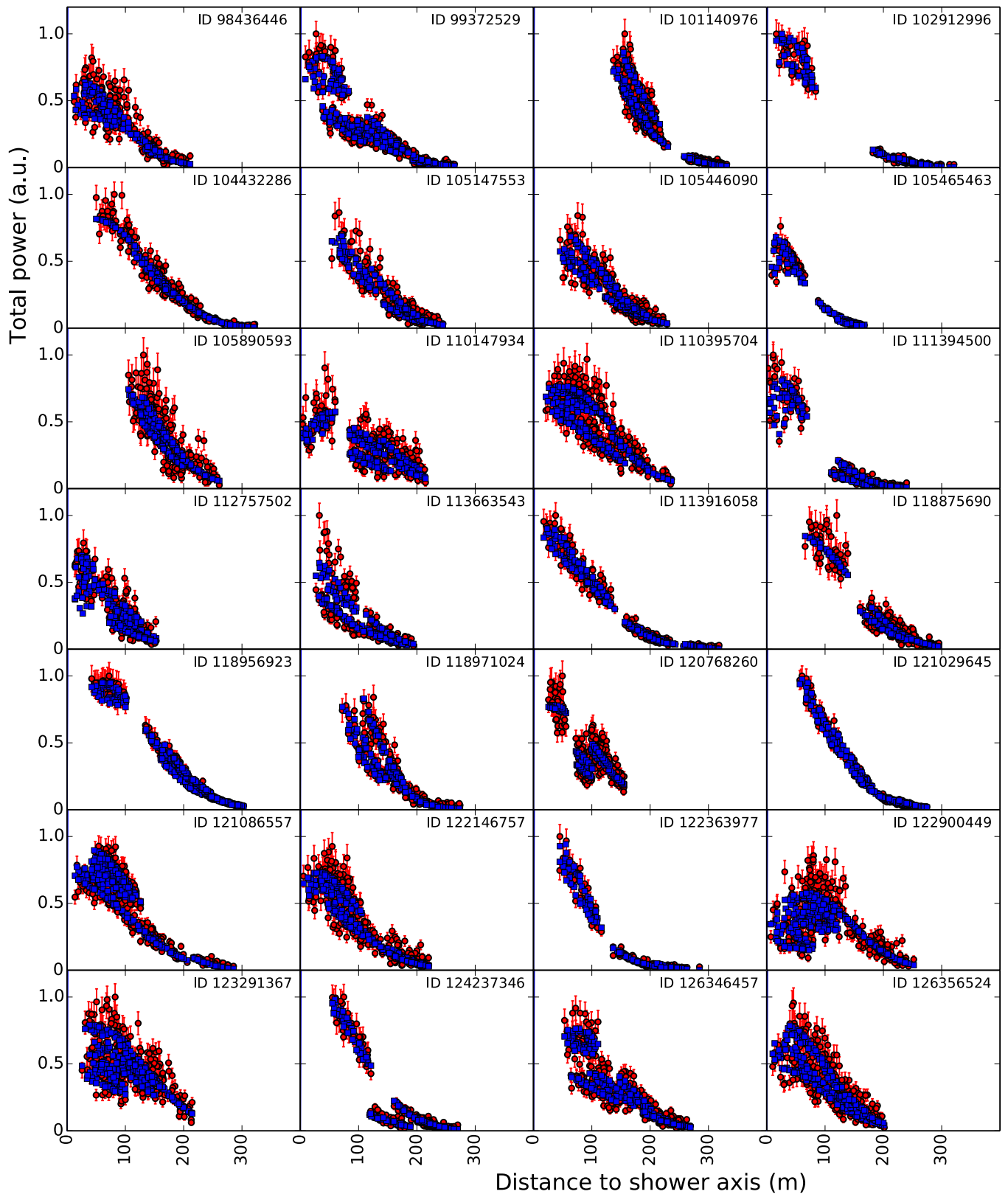
Extended Data Figure 1 | Fitted lateral distributions. Lateral distribution of radio-pulse power for all 118 measured showers (red circles) and the corresponding best-fitting CoREAS simulation (blue squares). The distance to the shower axis is the distance between the antenna and the axis of the air shower. Therefore, a value of 0 corresponds to an antenna that is located at the position where the shower axis reaches the ground. The ID numbers are unique values that are used to label the detected air showers. a.u., arbitrary units.
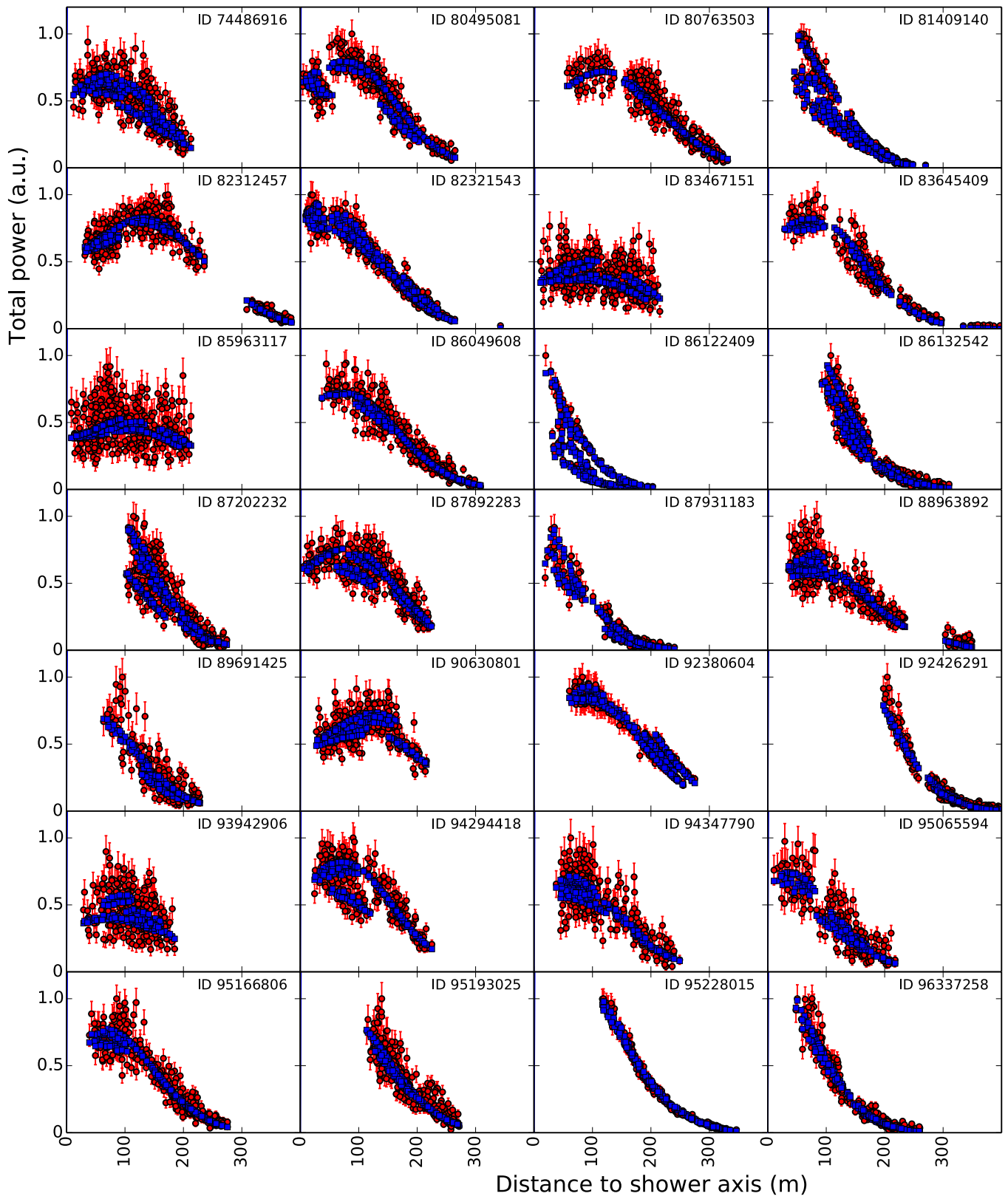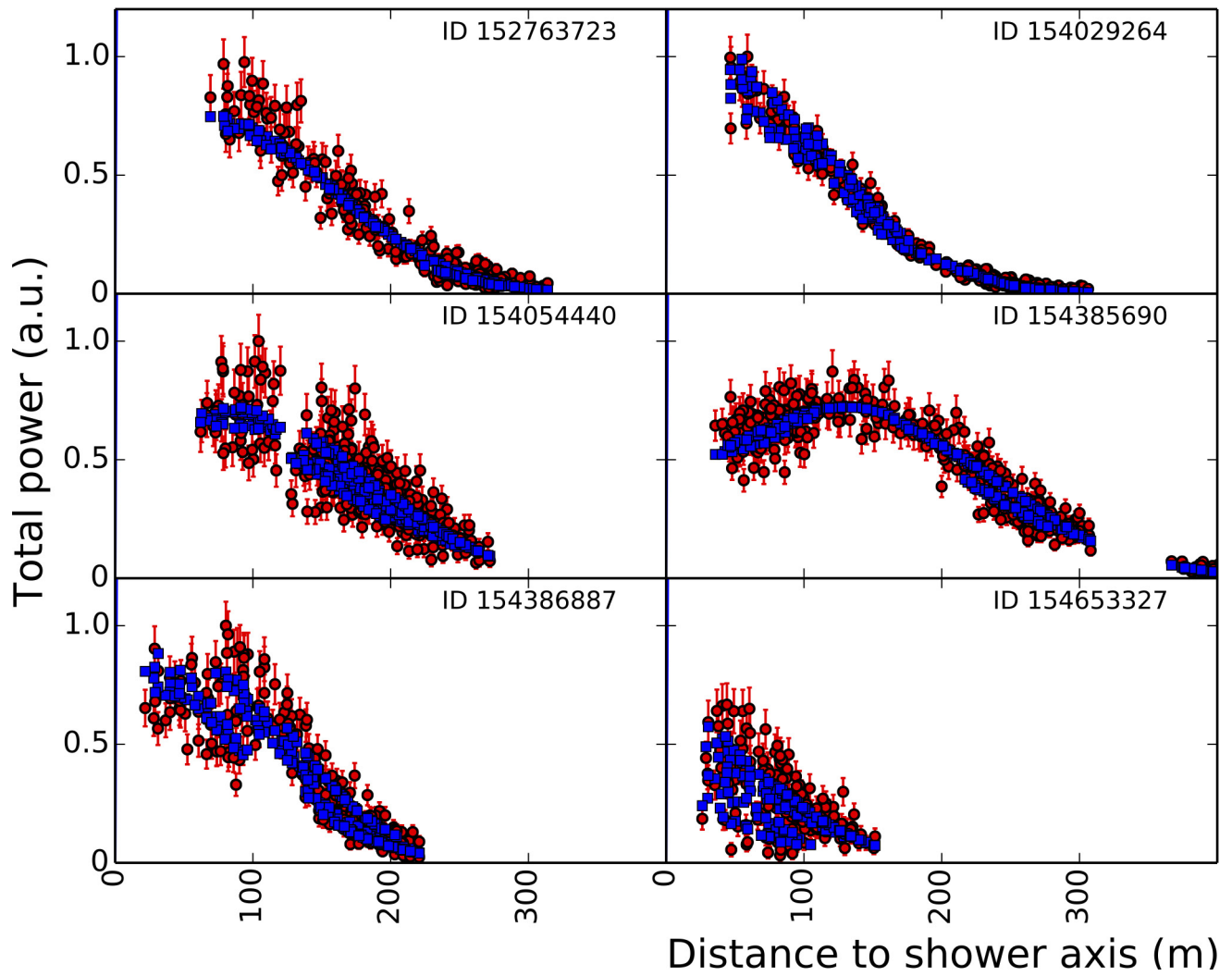
Extended Data Figure 2 | Fitted lateral distributions. Continuation of Extended Data Fig. 1.
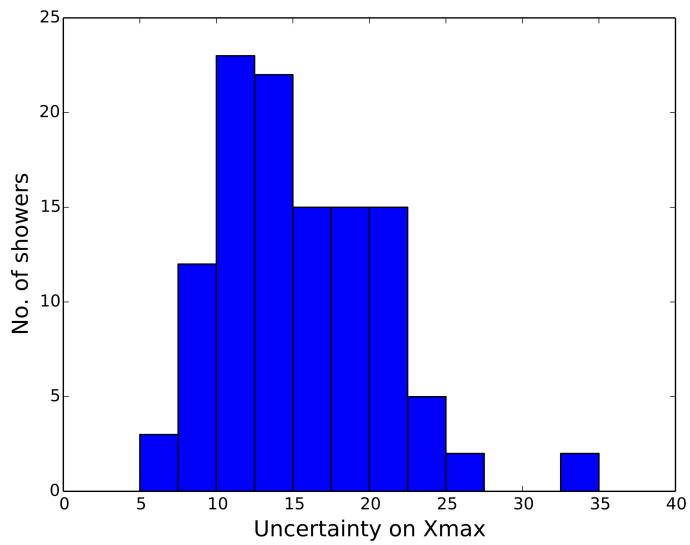
**Extended Data Figure 3 | Fitted lateral distributions.** Continuation of Extended Data Fig. 2.
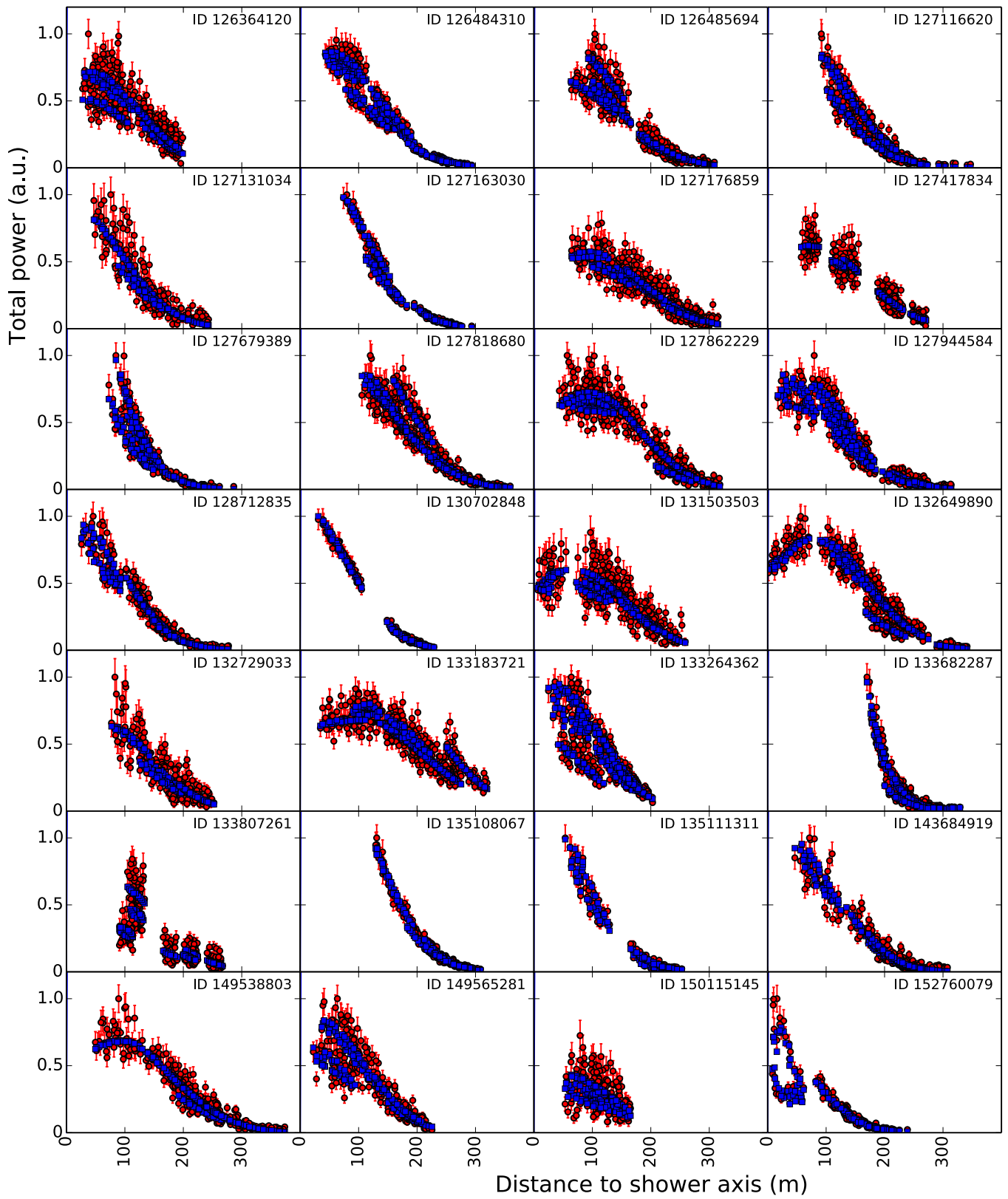
Extended Data Figure 4 | Fitted lateral distributions. Continuation of Extended Data Fig. 3.

Extended Data Figure 5 | Fitted lateral distributions. Continuation of Extended Data Fig. 4.

Extended Data Figure 6 | Distribution of uncertainty on X_{max}. The distribution of the uncertainty on X_{max} for all showers used in this analysis. The mean value is $16\,\mathrm{g\,cm^{-2}}$.
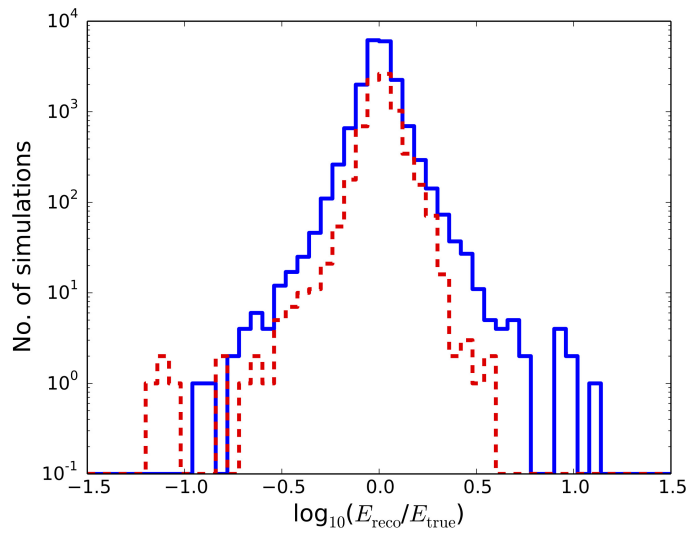
Extended Data Figure 7 | Energy reconstruction. Distributions of the ratio between true (E_{true}) and reconstructed (E_{reco}) energy for proton (blue solid line) and iron (red dashed line) showers. The two types of showers have a systematic offset of the order of 1%.

CORRECTIONS & AMENDMENTS

Corrigendum: A large light-mass component of cosmic rays at 10^{17}–$10^{17.5}$ electronvolts from radio observations

S. Buitink, A. Corstanje, H. Falcke, J. R. Hörandel, T. Huege, A. Nelles, J. P. Rachen, L. Rossetto, P. Schellart, O. Scholten, S. ter Veen, S. Thoudam, T. N. G. Trinh, J. Anderson, A. Asgekar, I. M. Avruch, M. E. Bell, M. J. Bentum, G. Bernardi, P. Best, A. Bonafede, F. Breitling, J. W. Broderick, W. N. Brouw, M. Brüggen, H. R. Butcher, D. Carbone, B. Ciardi, J. E. Conway, F. de Gasperin, E. de Geus, A. Deller, R.-J. Dettmar, G. van Diepen, S. Duscha, J. Eislöffel, D. Engels, J. E. Enriquez, R. A. Fallows, R. Fender, C. Ferrari, W. Frieswijk, M. A. Garrett, J. M. Grießmeier, A. W. Gunst, M. P. van Haarlem, T. E. Hassall, G. Heald, J. W. T. Hessels, M. Hoeft, A. Horneffer, M. Iacobelli, H. Intema, E. Juette, A. Karastergiou, V. I. Kondratiev, M. Kramer, M. Kuniyoshi, G. Kuper, J. van Leeuwen, G. M. Loose, P. Maat, G. Mann, S. Markoff, R. McFadden, D. McKay-Bukowski, J. P. McKean, M. Mevius, D. D. Mulcahy, H. Munk, M. J. Norden, E. Orru, H. Paas, M. Pandey-Pommier, V. N. Pandey, M. Pietka, R. Pizzo, A. G. Polatidis, W. Reich, H. J. A. Röttgering, A. M. M. Scaife, D. J. Schwarz, M. Serylak, J. Sluman, O. Smirnov, B. W. Stappers, M. Steinmetz, A. Stewart, J. Swinbank, M. Tagger, Y. Tang, C. Tasse, M. C. Toribio, R. Vermeulen, C. Vocks, C. Vogt, R. J. van Weeren, R. A. M. J. Wijers, S. J. Wijnholds, M. W. Wise, O. Wucknitz, S. Yatawatta, P. Zarka & J. A. Zensus

In this Letter, we omitted to cite preliminary results from the low-energy extension of the Pierre Auger Observatory, as presented at the International Cosmic Ray Conference 2015 (ref. 1). Figure 1 of this Corrigendum shows measurements of the average value of X_{max} for the Low Frequency Array (LOFAR), and earlier experiments using different techniques, now including the data from the Pierre Auger Observatory[1], specifically the contribution of A. Porcelli. Our values are in agreement with those of ref. 1 within systematic uncertainties.

1. The Pierre Auger Collaboration. The Pierre Auger Observatory: contributions to the 34th International Cosmic Ray Conference (ICRC 2015). *Proc. Sci.* **420**, http://pos.sissa.it/cgi-bin/reader/conf.cgi?confid=236. #420 (2015); preprint at http://arxiv.org/abs/1509.03732.
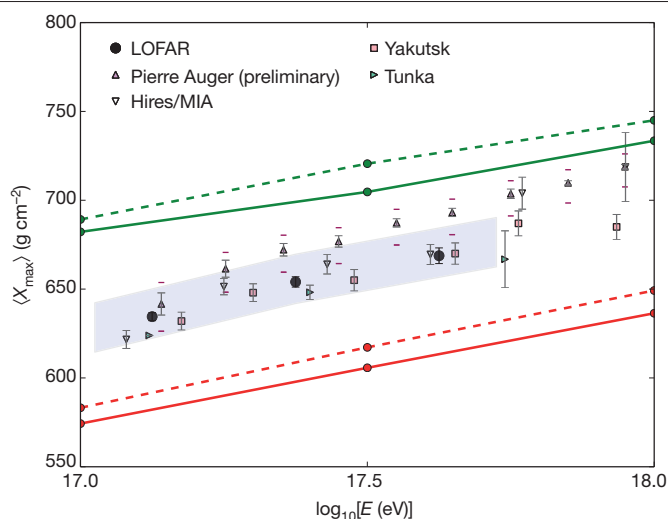
Figure 1 | This is an updated version of Fig. 2 of the original Letter, including the new data from ref. 1. Measurements of X_{max}. Error bars indicate 1σ statistical uncertainties and the shaded area represents the systematic uncertainty of the LOFAR results. The systematic uncertainties for Auger are indicated by the small horizontal lines above and below their data points.